PAPER

Check for updates

Magneto-fluorescent nanocomposites: experimental and theoretical linkage for the optimization of magnetic hyperthermia†

Kosmas Vamvakidis, [ID] Nikolaos Maniotis [ID] and Catherine Dendrinou-Samara [ID] *

Magneto-fluorescent nanocomposites have been recognized as an emerging class of materials displaying great potential for improved magnetic hyperthermia assisted by optical imaging. In this study, we have designed a series of hybrid composites that consist of zinc doped $Zn_xFe_{3-x}O_4$ ferrites functionalized by polyethylene-glycol (PEG8000) and an orange-emitting platinum complex $[Pt(phen)Cl_2]$. Experimental and theoretical studies on the optimization of their magnetically-mediated heating properties were conducted. PEG was assembled around particles' surface by two different approaches; *in situ* and post-PEGylation. PEGylation ensured the optimal distance between the magnetic core and Pt(II)-complex to maintain significant luminescence in the composite. The successful inclusion of the complex to the organic matrix was confirmed by a variety of spectroscopic techniques. A theoretical model was developed, based on linear response theory, in order to examine the composites' power losses dependence on their properties. Within this model, inter-particle interactions were quantified by inserting a mean dipolar energy term in the estimation of Néel relaxation time, and consequently, the size and concentration that maximize power loss were derived (20 nm and 4 mg mL^{-1}). Moreover, a decrease in the anisotropy of nanoparticles resulted in an increase in specific loss power values. Theoretical estimations are validated by experimental data when heating aqueous dispersions of composites in 24 kA m^{-1}, 765 kHz AMF for various values of concentration and size. Magnetic hyperthermia results showed that the theory-predicted values of optimum concentration and size delivered the maximum-specific loss power which was found equal to 545 W g^{-1}. By the present approach, a quantitative link between the particles' dipolar interactions and their heating properties is established, while opening new perspectives to nanotheranostic applications.

1. Introduction

Since the pioneering studies on the rational synthesis of individual magnetic nanoparticles (MNPs), the research focus has shifted towards the development of more complicated nanoarchitectures headed for biomedical multitasking applications.[1,2] These nanostructures of the next generation are composed of different functional modalities and are able to perform several tasks in parallel, such as simultaneous cancer imaging and therapy.[3–5] One of the most favorable dual-modality combinations is the integration of magnetic resonance imaging (MRI) with magnetic hyperthermia (MH) in a single probe.[6,7] However, other traditional diagnostic techniques have been seeking to endow combined properties with MH.

Optical fluorescence imaging (OFI) counts as an important real-time imaging technique that is used to study molecular effects,[8–10] while recently, it has been recommended for the imaging-guided surgery.[11,12] The most proposed optical imaging probes for OFI are fluorescent lipids,[13] quantum dots (QDs)[14–16] and organic dyes.[17–19] These systems show much promise but suffer from one or more shortcomings. Photobleaching and low chemical stability are some of the major drawbacks of organic dyes functionalized with ferrite nanoparticles.[20,21] Even though QDs present high quantum yields, they are considered toxic to the human body.[22,23] Lately, photoluminescent metal complexes (PTMCs) have drawn much attention as imaging agents due to their long-term optical stability.[24] These complexes are able to emit intense light *via* a metal-to-ligand charge transfer (MLCT) process and can serve as long-living dyes in various aqueous solutions. Among PTMCs, square planar platinum(II) com-

Laboratory of Inorganic Chemistry, Department of Chemistry, Aristotle University of Thessaloniki, 54124 Thessaloniki, Greece. E-mail: samkat@chem.auth.gr
†Electronic supplementary information (ESI) available. See DOI: 10.1039/d1nr00121c

plexes display interesting photophysical properties, appropriate for OFI. Since the approval of cisplatin for the treatment of various cancers, Pt-complexes have been applied as theranostics through encapsulation into host matrices at the surface of the individual and/or clustered MNPs.[25–27]

The efficacy of magnetic hyperthermia is usually measured using specific loss power (SLP), which is the power released by MNPs in the form of heat. MH depends on many factors such as magnetic field characteristics (frequency and amplitude), MNPs composition and concentration, size, saturation magnetization and magnetic anisotropy, internal structure and hydrodynamic behavior. In addition, dipolar interactions can also play an important role in MH. By fine-tuning the external field's parameters with MNP properties, it is possible to increase the efficiency of the experiment by orders of magnitude. Thus, a comprehensive analysis of SLP becomes a multi-parametric task that requires modeling the experimental conditions and properties of involved materials.[28]

The synergistic combination of OFI-MH in a single nano-composite can exploit both the high sensitivity of OFI for real-time monitoring of the ongoing cancer therapy and the local heat-up of MH for treatment. Such hybrid magneto-fluorescent nanostructures are rarely designed, while theoretical studies on their induction heating properties are still rare. During the preparation of this manuscript, Das *et al.* presented the development of a novel magnetoluminescent nanocomposite.[29] Their research centered on the grafting procedure of luminophores on the particle core but not on the optimization of hyperthermia performance.

An extra concern about the synthesis of an OFI-MH dual agent arises from the presence of MNPs near the environment of the imaging probe, which can cause quenching of luminescence *via* an energy transfer process.[15,28–31] To overcome this effect, the formation of a stable silica (SiO_2) shell around MNPs' surface prior to the introduction of the fluorescent molecule has been proposed.[32–34] However, the precise control of the thickness of SiO_2 is complicated,[31] while Si–O–Si bonds are prone to hydrolysis when exposed to harsh environments, such as highly saline conditions encountered in biological media.[35–37] Another drawback of silica is the possible reduction of magnetization of the produced OFI-MRI composites due to a large amount of magnetically inert organic layer.[38,39]

In the present study, we investigate an OFI-MH dual agent based on the combination of MNPs and PTMCs. In particular, a series of doped zinc ferrites MNPs ($Zn_xFe_{3-x}O_4$, x = 0.3, 0.4, 0.45, 0.53) of small size and high M_s values have been synthesized,[40] as well as the orange-emitting complex [Pt(phen)Cl₂]. The Pt-phenanthroline complex presents π–π stacking in the solid-state, resulting in electronic interactions associated with Pt⋯Pt orbital overlap.[41] Apart from its optical properties, it demonstrates cytotoxic, apoptotic effects and is capable of suppressing tumor formation in a dose-dependent manner.[42] To anticipate the quenching issue we excluded the use of silica and the hybrid composites were surface-functionalized with polyethylene glycol (PEG) that also acted as an organic template for the absorption of the Pt-complex. PEG has the advan-

tage of the highest solubility and smallest hydrodynamic size among other coatings (dextran, silica, *etc.*) while PEGylation effectively eliminates cytotoxicity and provides protection against sedimentation for long. The physicochemical characterization of the composites was conducted to verify their successful formation and stability over time. To understand their in-depth performance as MH agents, we conducted a theory-driven optimization of SLP values that predicted a strong influence of dipolar interactions on SLP, being capable of both increasing and decreasing it, while its dependence on other MNP parameters such as size, anisotropy and concentration was also revealed. Those properties were tailored by using the linear response theory (LRT) combined with a mean-field model. The heating evaluation of these hybrid magneto-fluorescent nanocomposite systems, accompanied by a comprehensive theoretical analysis for optimization, is presented for the first time and serves as a strategy for their potential employment as nanotheranostic agents.

2. Materials and methods

2.1 Materials

All the required reagents were of analytical grade and were used without any further purification: iron(III) acetylacetonate $Fe(C_5H_7O_2)_3$ [Fe(acac)₃, Fluka, ≥97%], zinc chloride $ZnCl_2$ (Fluca, ≥97%), 1,2-propylene glycol $C_3H_8O_2$ (PG, Sigma, ≥98%), triethylene glycol $C_6H_{14}O_4$ (TrEG, Sigma ≥98%), tetra-ethylene glycol $C_8H_{18}O_5$ (TEG, Sigma, ≥99%), potassium tetra-chloroplatinate(II) K_2PtCl_4 (Sigma, ≥99.99%), 1,10-phenanthro-line $C_{12}H_8N_2$ (phen, Sigma, ≥99%), sodium chloride NaCl (Sigma, ≥99%), hydrochloric acid HC1 (Sigma, ACS reagent, 37%), polyethylene glycol-8000 (PEG-8000, Alfa Aesar), ethanol C_2H_5OH (Bruggemann, GmbH, ≥96%), dimethyl sulfoxide C_2H_6OS (DMSO, Sigma ≥99.7%).

2.2 Synthesis of $Zn_xFe_{3-x}O_4$ MNPs

For the preparation of the ferrite MNPs, a microwave-assisted polyol process and a modified solvothermal method were adopted that are described extensively in our previous works.[39,43] Briefly, Fe(acac)₃ (2.7 mmol) and $ZnCl_2$ (1.3 mmol) were dissolved in 0.9 mmol of polyol (PG, TrEG, TEG and PEG8000) and the mixture transferred to an autoclave. After the reaction, at 240 °C for 30 min for the microwave approach, the autoclave was cooled to room temperature and the particles were washed three times with ethanol and isolated by centrifugation (5000 rpm). According to the polyol that was involved, the three samples were labeled as $Zn_xFe_{3-x}O_4$@PG, $Zn_xFe_{3-x}O_4$@TrEG and $Zn_xFe_{3-x}O_4$@TEG. For $Zn_xFe_{3-x}O_4$@PEG, a solvothermal approach was adopted. The solvothermal reaction occurred at 200 °C for 24 h, while the isolation of MNPs was performed for the above samples.

2.3 Synthesis of [Pt(phen)Cl₂]

The Pt-complex was prepared according to the literature procedure.[44] Potassium tetrachloroplatinate(II) (0.05 mmol), 1,10-

phenanthroline (0.05 mmol), NaCl (67 mg) and HCl (0.1 ml) were dissolved in 50 ml of water in a 100 ml round-bottomed flask. A stir bar was added and the flask was attached to a condenser and set to reflux for 3 h. The light yellow product that precipitated was filtered out, washed with hot water and dried under vacuum; yield 80%.

2.4 Absorption of [Pt(phen)Cl₂] onto PEGylated MNPs

First, in a stable aqueous (10 mL) suspension of the polyol-coated MNPs (15 mg), 5 mL of the aqueous solution of PEG (100 mg) was added. The mixture was left to stir for 24 h during which PEG gradually self-assembled on the surface of the particles. The PEGylated MNPs were magnetically isolated, washed three times with ethanol, and dried under vacuum. In the second step, PEGylated MNPs (15 mg) were dispersed in distilled water (15 mL), where [Pt(phen)Cl₂] (15 mg) was added and the mixture was stirred at room temperature. After 24 h, the formed nano-molecular composites were collected using a permanent magnet, washed three times with ethanol and dried at room temperature under vacuum.

2.5 Magnetic hyperthermia

For magnetic hyperthermia (MH) measurements, a commercial 2-turn solenoid coil (25 mm in diameter and 10 mm in height) resonating at 765 kHz capable of generating a homogenous field in a volume of approximately 5 cm³, ensuring that the whole sample was immersed in a region with a uniform amplitude, was used. The applied alternating magnetic field amplitude was set at 24 kA m⁻¹ that is a typical condition employed in MH experiments.[45] The desirable magnetic field could be achieved by adjusting the coil current. Moreover, the cooling system is based on a constant flow of water, which is automatically adjusted in order to keep the temperature of the water flowing at a specific value. It is worth noting that the presence of cooling water flowing through the coil keeps the latter at a constant temperature to avoid overheating. Water temperature was found to be 11 °C while the room temperature was 25 °C. A time step of 0.4 s was selected between consecutive temperature recordings and the total experimental process lasted 1200 s, composed of heating (field on) and cooling (field off) parts. A fiber-optic thermometer system was used to record the temperature of the samples with an accuracy of ±0.1 °C. All the hyperthermia measurements were performed under similar conditions, *i.e.*, the sample holder (glassy vial) and its volume (1 mL), its position within the magnetic field, MH measurement time (1200 s including 600 s of sample heating and 600 s of cooling), and at the same alternating magnetic field (AMF) frequency and amplitude.

2.6 Characterization techniques

The primary particle size and morphology were determined by conventional transmission electron microscopy (TEM) images obtained with a JEOL JEM 1010 microscope operating at an acceleration voltage of 100 kV. For TEM observations, we used suspensions of nanoparticles deposited onto carbon-coated copper grids. The elemental composition of primary MNPs

was estimated *via* ICP-AES analysis (iCAP 6300, Thermo Scientific). The hydrodynamic size and surface charge of the composites were determined by dynamic light scattering (DLS) and zeta potential measurements, carried out at 25 °C, utilizing a Nano ZS Malvern apparatus. The elemental composition of samples was tested using scanning electron microscopy (SEM, JEOL 840A), where energy dispersive X-ray spectrometry (EDS) spectra were obtained. Thermogravimetric analysis (TGA) was carried out from room temperature to 900 °C at a heating rate of 10 °C min⁻¹ under an N₂ atmosphere on a SETARAM SetSys-1200 instrument. Fourier transform infrared spectroscopy (400–4000 cm⁻¹) was performed on a Nicolet FT-IR 6700 spectrometer, (Thermo Electron, Waltham, MA, USA), with pellet samples prepared using KBr. UV-Visible measurements were performed on a spectrophotometer (2001 Hitachi, Kagoshima, Japan). The emission spectra were measured on a Horiba fluorescence spectrometer equipped with a powder sample holder. The light source was a 450 W xenon arc lamp (220–1000 nm) and the detector was a red-sensitive Hamamatsu R928 photomultiplier tube. Magnetic measurements on the samples in powdered form were performed with a vibrating sample magnetometer (Oxford Instruments 1.2 H/CF/HT VSM). The maximum-applied field was equal to 1 T with a field rate of 0.5 T min⁻¹.

3. Results and discussion

3.1 Design and formation of composites

Based on our previous results,[39] primary doped zinc ferrites $Zn_xFe_{3-x}O_4$ ($0.3 \leq x \leq 0.5$) MNPs were isolated using a microwave-assisted polyol process in the presence of 1,2-propylene glycol (PG), triethylene glycol (TrEG) and tetraethylene glycol (TEG). Each polyol resulted in a different Zn^{2+} doping level according to its reductive ability and further ensured the dispersion of MNPs in water. Fundamentally, the reducing ability of polyols depends on their molecular weight; as the molecular weight of polyol decreases, b.p. decreases, and the reducing ability is increased.[46] The composition of three synthesized $Zn_xFe_{3-x}O_4$ MNPs was estimated by ICP-AES as $Zn_{0.6}Fe_{2.4}O_4$, $Zn_{0.45}Fe_{2.55}O_4$, and $Zn_{0.3}Fe_{2.7}O_4$ for TrEG, PG, and TEG, respectively. The average nanoparticle sizes (d_{TEM}) were found 14, 11 and 9 nm for the samples: S_1-$Zn_{0.45}Fe_{2.55}O_4$@PG, S_2-$Zn_{0.6}Fe_{2.4}O_4$@TrEG and S_3-$Zn_{0.3}Fe_{2.7}O_4$@TEG, respectively (Fig. S1†).[39] The relatively small size variations are attributed to the different molecular weight of polyol that was used at each synthetic protocol. Another sample (S_4) of zinc ferrite MNPs was solvothermally prepared in the presence of PEG solely performing a triple role: solvent, reducing agent and coating. Fig. 1 shows the XRD pattern and the TEM image of S_4-$Zn_{0.53}Fe_{2.47}O_4$@PEG with an average size (d_{TEM}) 20 nm, while further physicochemical properties are given in ESI (ESI, Fig. S1†).

Post-PEGylation has been attempted for S_1–S_3, where PEG was self-assembled on particles' surface after synthesis, while *in situ* PEGylation, where PEG was attached on the surface
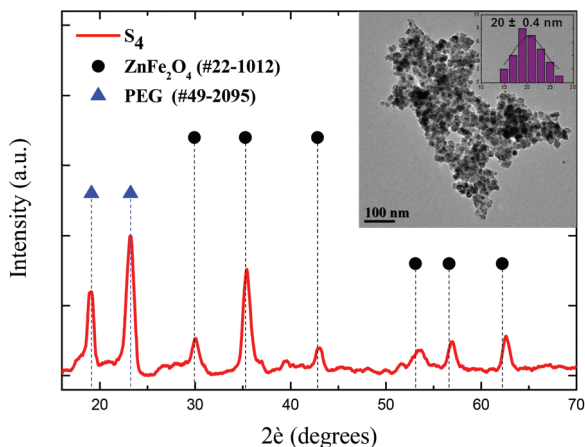
Fig. 1 All the peaks of the XRD pattern are well-matched with the standard JCPDS data of $ZnFe_2O_4$, while the two distinct peaks at 19° and 23° confirm the presence and crystallization of PEG on the surface. The bright-field TEM image of the sample (S_4) clearly shows nearly spherical nanoparticles covered by PEG.

during synthesis, was utilized for sample (S_4). After PEGylation, all samples ($S_{1–4}$) were able to function as absorbents for the platinum complex. The poor solubility of the complex in water was the driving force that facilitated its incorporation into the polymer's hydrophobic chains. Immobilization of the prepared complex on the PEGylated MNPs resulted in the formation of the desired nanocomposites named for clarity as S_b@Pt, (b = 1, 2, 3, 4). The process for the synthesis of novel hybrid magneto-fluorescent agents is presented in Scheme 1A and B, respectively.

3.2 Characterization of composites

The successful incorporation of the complex into PEG chains was evidenced from EDS, FT-IR, UV-Vis and fluorescence spec-

troscopy measurements. Compositional analysis of the composites was estimated using energy-dispersive X-ray (EDS) spectroscopy. Besides the detection of zinc and iron, peaks of platinum substantiated the presence of the complex. Furthermore, the relative atomic abundance (%) obtained from the spectra were S_1 (1.07%), S_2 (1.74%), S_3 (0.80%) and S_4 (3.75%) (ESI, Fig. S2†). The differential Pt content is attributed to the variation in PEG content as indicated by DLS measurements, given in the context below.

FT-IR spectra of the composites are presented in Fig. 2, where several bands are identified belonging to both Pt-complex and organic coating as well as to ferrite MNPs. The high-frequency bands located in 3082 and 3054 cm^{-1} regions are assigned to symmetrical (ν_s) and asymmetrical (ν_{as}) stretching vibrations of CH_3 and CH_2 of PEG. Characteristic peaks of the phenyl ring, such as the out-plane bending vibration of the C–H bond, have been shifted slightly, appearing at 712 cm^{-1} in the composites and 717 cm^{-1} in the complex.[47] The peak at 570 cm^{-1} corresponds to the motion of oxygen with respect to cations in T_d and O_h sites of the spinel structure, demonstrating the existence of MNPs in the composites.[48] Fig. 5S† presents the thermogravimetric analysis (TGA) of the hybrid nanocomposites. The presence of a double layer is common for all samples. The first step at about 420 °C is attributed to the initial polyol coating, while the second one at about 730 °C stems from PEG polymer. The cumulative contents were found to be 58, 44, 39 and 66 w/w%, for S_1@Pt to S_4@Pt, respectively.

Dynamic light scattering (DLS) of aqueous dispersions of four composites was carried out to investigate their hydrodynamic diameter and ζ-potential (Fig. S3†) The diameters of the samples prepared by the post-PEGylation route ($S_{1–3}$@Pt) was found to be similar, ranging from 349 to 404 nm, while for the *in situ* PEGylated sample (S_4@Pt) the size was greater (620 nm). Owning to the electrical neutrality of PEG, the zeta potential of the samples was quite negligible. However, par-
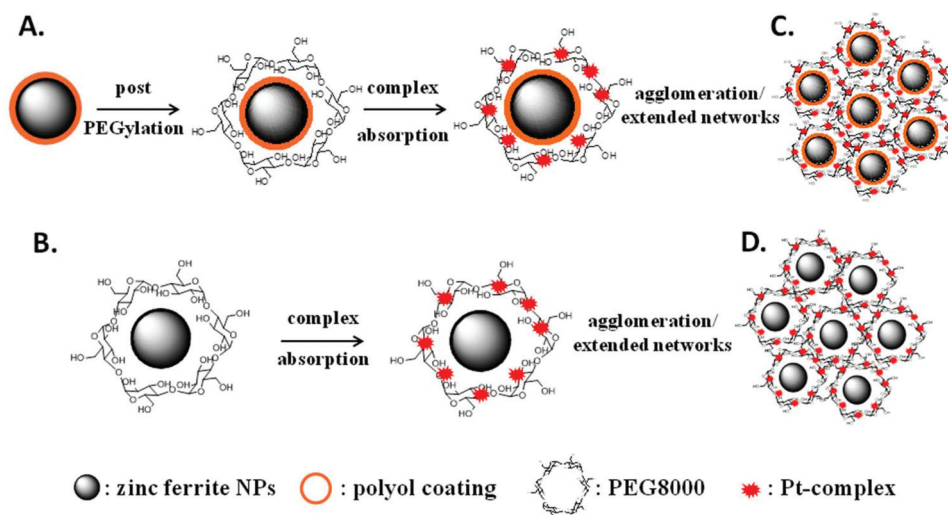
Scheme 1 Illustration of the design of hybrid nano-molecular composites. Firstly, post (1) or *in situ* (2) PEGylation was promoted on particles' surface and, finally, the Pt-complex was absorbed into the hydrophobic polymer's chains.
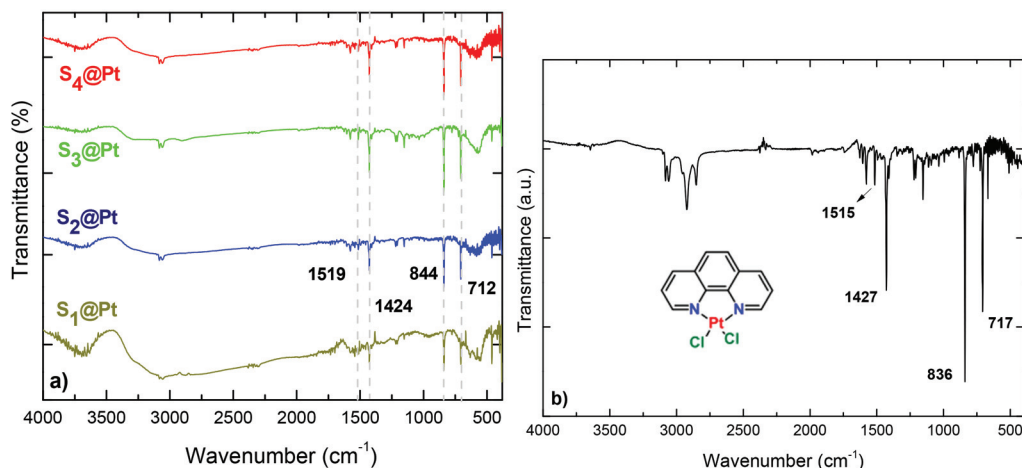
Fig. 2 FT-IR spectra of (a) hybrid magneto-fluorescent composites in comparison with the (b) synthesized platinum complex, [Pt(phen)Cl₂].

ticles retained their aqueous dispersion ability, thanks to the steric stabilization stemming from polymer chains. As such, and as expected, PEGylation led to an increase in size and concomitantly to a reduction in the magnitude of surface charge. Moreover, the presence of PEG between Pt complexes and zinc ferrite MNPs makes the whole conjugate stable in biological solutions without serious toxic effects.[49] The increased hydrodynamic sizes in comparison with sizes from TEM can be considered as a result of the large organic content and swelling of PEG in the water, while agglomeration/extended network formation cannot be excluded, as shown in Scheme 1C and D.[50]

The electronic absorption spectra of magneto-fluorescent composites together with the pure Pt-complex in DMSO are shown in Fig. 3a. The Pt-complex exhibits the characteristic intraligand π–π* transition of phenanthroline at 365 nm and an extra shoulder at 388 nm, that are assigned to d(Pt)–π*(phenanthroline) charge transfer.[35] On the other hand, PEGylated MNPs in the same concentration show no typical absorption in the spectrum range studied (inset of Fig. 3a). Only an expo-

nential decay is observed originating from the Rayleigh scattering of the electromagnetic spectrum.[51] In contrast, hybrid composites, owning to the absorbed Pt-complex, displayed weak shoulders which disturbed their exponential decay, and confirm the successful attachment of [Pt(phen)Cl₂] to PEGylated MNPs.

As the absorbance of the composites is derived solely from the presence of the complex, its concentration in each sample can be calculated from their absorbance at 388 nm. Firstly, a calibration curve was obtained from the plot of the complex concentration *versus* the ratio of the integrated intensities of the absorption band (Fig. 3b). After that, the absorption of the composites was recorded and the amount of the complex was obtained from the experimental curve. No significant differences were detected in the concentration of the complex in post-PEGylated samples (0.09 mM) and that is the reason why all values are represented in the same red dot. For the *in situ* PEGylated composite, the amount was higher (green dot: 0.16 mM), in accordance with the EDS analysis.
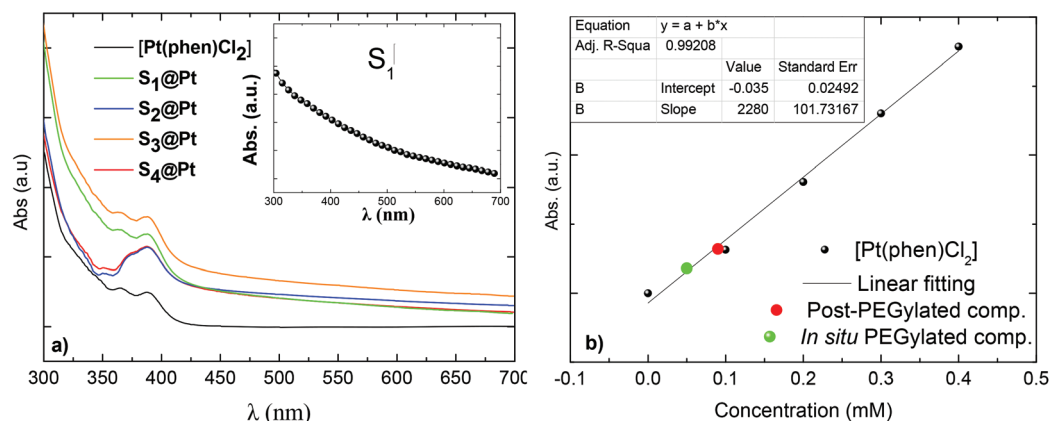

Fig. 3 (a) Absorption spectra of the composites and the Pt-complex diluted in DMSO, (inset) indicative spectrum of the primary zinc ferrite MNPs coated by propylene glycol (S₁) and (b) calibration curve (black circles) and amount of Pt-complex of post-PEGylated (red circle) and *in situ* PEGylated (green circle) composites.

The stability of composites before and after each hyperthermia measurement was further evaluated by UV-Vis studies in order to assess the possible leaching of the complex from PEGylated MNPs. Thus, after each hyperthermia measurement, hybrid composites were magnetically isolated by a permanent magnet ($Nd_2Fe_{14}B$) and the absorption of the supernatant was monitored (ESI, Fig. 4S†). Results disclosed that there was no conspicuous emission remaining in solutions, and as such, there was no loss of the complex during hyperthermia measurements. The above experimental observations provided through evidence for the compact nature of the hybrid magneto-fluorescent composites.

3.3 Fluorescence properties of composites

Emission spectra of [Pt(phen)Cl₂] and nano-molecular composites were recorded under an excitation λ_{exc} = 400 nm at room temperature in the wavelength range of 450–750 nm (Fig. 4a). A strong emission in the visible spectral regime from the platinum complex is observed at 637 nm due to an efficient energy transfer from phenanthroline to platinum(II) ions.[52] Upon absorption of the complex onto the surface of MNPs, the luminescence intensity of the composites was decreased compared to that of the pure complex due to the visible absorption of the magnetic nanoparticles. However, the interlayer of PEG/polymer effectively reduces the total fluorescence-quenching of the complex and fluorescence remains at acceptable levels.[53]

Indicative digital photos of the composite S₃@Pt were taken first under daylight and then under ultraviolet with the excitation wavelength of 365 nm (Fig. 4b–e). Under daylight, the aqueous dispersion showed a brown color (Fig. 4b), while under UV excitation an orange color was indicated (Fig. 4d),
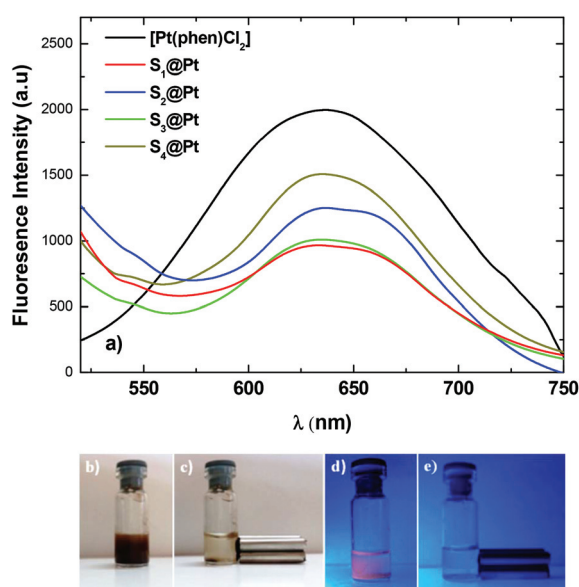

Fig. 4 (a) Solid-state fluorescence emission spectra (λ_{ex} = 400 nm) of the composites and the Pt-complex. Digital pictures of (b) aqueous solution of the composite S₃@Pt under daylight, (c) aqueous solution of the composite under magnetic field and under daylight, (d) and (e) corresponding pictures under UV excitation (λ_{exc} = 365 nm).

which is in good agreement with the fluorescent properties of the system. Also, the magneto-fluorescent composite completely separated to the side of the vial with a magnet in 5 min and the solution became completely clear (Fig. 4e). The rapid magnetic separation is attributed to the cooperative magnetophoresis effect of the applied external magnetic field induced agglomeration among MNPs.[54]

3.4 Magnetic properties of composites

Magnetic measurement data on the samples S₁@Pt, S₂@Pt, S₃@Pt, and S4@Pt are shown in Fig. 5, where the values of saturation magnetization M_s were found equal to 53 (100), 52 (96), 66 (114) and 77 (126) emu g⁻¹, respectively. The corresponding net magnetization values, per gram of magnetic core, at the maximum field applied (1 T) are also reported in brackets. Despite the addition of the Pt-complex, M_s values are still among the highest values reported for functionalized Zn ferrite MNPs by using polyols as surfactants.[55–59] The central part of magnetization *versus* field cycles is presented in ESI in Fig. S7† together with a table (Table S1†) where the values of a coercive field are reported for all samples.

Magnetic anisotropy is an intrinsic property that affects drastically MNPs magnetic and heating properties. In order to estimate the effective anisotropy constant K of the samples, the magnetization curves using the law of approach to saturation[60] were fitted as:

$$M(H) = M_S\left(1 - \frac{\alpha}{H} - \frac{\beta K^2}{M_S^2 H^2}\right) + \gamma H \qquad (1)$$

where β is equal to 4/15 for magnetic nanoparticles with uniaxial anisotropy, and α, γ are fitting constants. The fitting magnetization curves at saturation are shown in the inset of Fig. 5. All experimental data could be fitted into eqn (1) with R-squared values higher than 98%. The K values were found after fitting equal to 16, 23, 10 and 5 kJ m⁻³ for S₁@Pt, S₂@Pt, S₃@Pt and S₄@Pt, respectively, and are consistent with the anisotropy values found in the literature for zinc-doped magnetite nanoparticles.[61–63] The S₄@Pt presented the highest saturation magnetization and the lowest anisotropy, a result that is attributed to its larger magnetic core size compared to the other samples (20 nm). Upon decreasing the size of the nanoparticles, the surface effects become progressively dominant. Disorder in lattice symmetry close to and at the surface appears and disordered spins at the surface induce additional anisotropy[64,65] provoking impediment to the magnetization progress. It should also be mentioned that in an assembly of magnetic nanoparticles with a certain size distribution, the distribution of anisotropy constants exists.[66] However, the obtained values have been considered as mean values for an effective anisotropy in all calculations.

3.5 Evaluation of magnetic hyperthermia properties

For magnetic hyperthermia experiments and calorimetric measurements of SLP, aqueous dispersions of all samples with a frequently used concentration[67–69] of 2 mg mL⁻¹ were initially prepared. All the hyperthermia measurements were performed
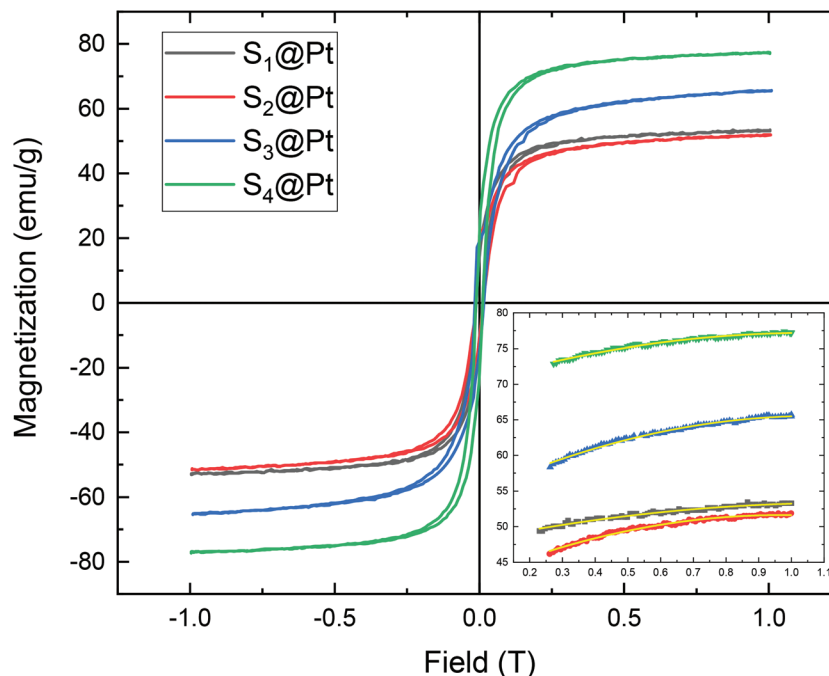
Fig. 5 The magnetization *versus* the magnetic field, *M*(*H*), dependence for the MNP samples after different degrees of polyol functionalization. The magnetization curves were obtained at 300 K. The inset is the fitted magnetization-field data with the law of approach described by eqn (1). The symbols, following the same color indexing to the entire *M*(*H*) curves, are the experimental data and the yellow lines are the fittings.

under similar conditions, *i.e.*, the sample holder (glassy vial) and its volume (1 mL), its position within the magnetic field, and MH measurement time (1200 s including 600 s of sample heating and 600 s of cooling), the same AMF frequency and amplitude. Magnetic hyperthermia curves for all samples, with and without the addition of the Pt-complex, are presented in Fig. 6a. Note that the optical fiber endures up to 90 °C, and thus, for safety reasons, the MH device was turned off when the temperature was approaching 60 °C. This is the case for sample S_4, where due to its high heating rate, the AMF exposure time was shorter than 600 s. It is obvious that after the addition of Pt-complex a decrease of the heating efficiency in all samples was triggered, while none of the magneto-fluorescent composites entered the magnetic hyperthermia therapeutic window of 41–45 °C.

In order to quantify the heating diminution, the resulting SLP values were estimated from eqn (2):

$$\text{SLP} = C_{\text{p}} \frac{m_{\text{f}}}{m_{\text{MNPs}}} \frac{\Delta T}{\Delta t} \qquad (2)$$

where C_{p} is the specific heat of the ferrofluid, m_{f} is the ferrofluid mass, m_{MNNPs} is the mass of the magnetic material and $\frac{\Delta T}{\Delta t}$ the initial (calculated in the first 100 s) slope of temperature increase curves. For reasons for comparison, in addition to SLP, the intrinsic loss power (ILP) is also reported taking into account the frequency f and amplitude H_0 of the excitation field. ILP is given as ILP = SLP/($H_0^2 \cdot f$). According to the results shown in Fig. 6b, the reduction of SLP values is evidenced for all samples. It is worth mentioning that the

superior magnetic performance of samples S_4 and S_4@Pt is also reflected through their heating performance resulting in higher heating rates than that for all the other samples. More specifically, for sample S_1, it is decreased from 252 W g^{-1} (ILP = 0.57 nHm^2 kg^{-1}) to 86 W g^{-1} (ILP = 0.19 nHm^2 kg^{-1}), for sample S_2 from 196 W g^{-1} (ILP = 0.44 nHm^2 kg^{-1}) to 40 W g^{-1} (ILP = 0.10 nHm^2 kg^{-1}), for sample S_3 from 308 W g^{-1} (ILP = 0.70 nHm^2 kg^{-1}) to 190 W g^{-1} (ILP = 0.43 nHm^2 kg^{-1}) and for sample S_4 from 380 W g^{-1} (ILP = 0.86 nHm^2 kg^{-1}) to 213 W g^{-1} (ILP = 0.48 nHm^2 kg^{-1}). This initial evaluation motivated us to develop a theoretical approach to simultaneously optimize SLP and accurately interpret the experimental results. Thus, the efficiency of the samples was further investigated under a theoretical prism.

3.6 Coupled theoretical and experimental investigation

3.6.1 Modelling. Heating optimization of MNPs is apparent since it is necessary to keep MNPs heating efficiency at a satisfactory level to enter the MH window. A comprehensive analysis of SLP values becomes a multi-parametric task that requires complete knowledge of the applied magnetic field parameters and the intrinsic properties of magnetic nanoparticles such as their size and anisotropy. Hitherto, these requirements have been obtained from experimental data and have been applied in the theoretical calculation of SLP. Additionally, dipolar interactions are also to be taken into account. Since, in a realistic colloidal dispersion of MNPs, in addition to the existence of particle aggregation, there may always exist a degree of dipolar interactions even in well-dispersed samples.[70] Those interactions are considered impor-
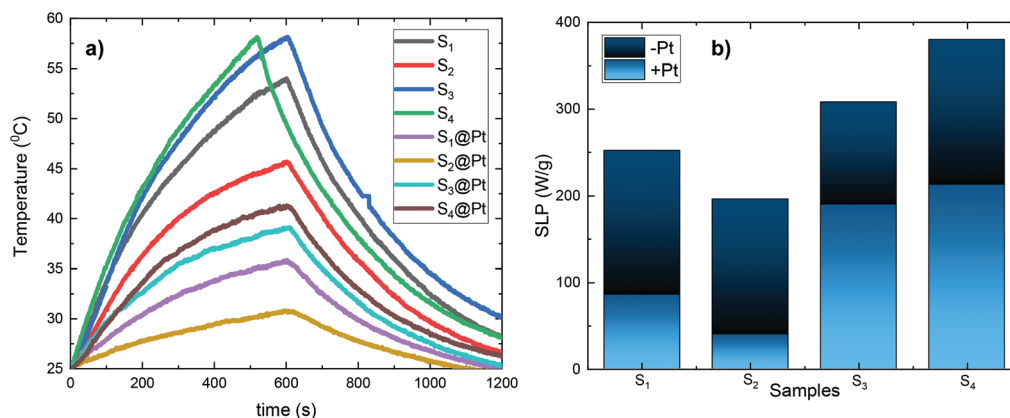
Fig. 6 (a) Heating sequence curves of the PEGylated MNPs and hybrid composites after 600 s of MH treatment and 600 s of sample cooling. The concentration was the same for all samples and equal to 2 mg mL^{-1}, (b) SLP values of samples before (−Pt) and after (+Pt), the absorption of the complex [Pt(phen)Cl$_2$]. An obvious reduction in SLP is observed for all samples.

tant as sometimes they modify the SLP of the system by up to two orders of magnitude.[71]

When superparamagnetic MNPs of volume V are exposed to low AMFs of frequency f and amplitude H_0 their volumetric power dissipation P is given by the linear response theory (LRT):[72]

$$P = \pi\mu_0\chi_0 H_0^2 f \frac{2\pi f \tau}{1 + (2\pi f \tau)^2} \quad (3)$$

where χ_0 is the static magnetic susceptibility of MNPs defined as $\chi_0 = \mu_0 M_s^2 V/3k_B T$ and τ is the relaxation time due to Brownian and Néel mechanisms of magnetic moment relaxation. When dipolar interactions are non-negligible τ_N is given by the following equation:[73]

$$\tau_N \approx \exp(\sigma + \gamma\sigma^2) \quad (4)$$

where σ is the anisotropy barrier KV and γ the mean energy due to the dipole interactions given by:

$$\gamma = \frac{N}{10}\left(\frac{\mu_0 M_s^2 V}{4\pi K}\right)^2 \frac{1}{D^6} \quad (5)$$

In eqn (4), N is the total number of MNPs and D the mean distance between MNPs. The MNPs number is given by:

$$N = \frac{c \times \dfrac{V_{\text{ferrofluid}}}{V_{\text{NP}}}}{\rho_{\text{NP}}} \quad (6)$$

where $V_{\text{ferrofluid}}$ is the volume of the solution containing the MNPs, also termed ferrofluid, and c and ρ_{NP} are the MNPs concentration and density, respectively. The mean distance between MNPs is equal to:

$$D = \left(\frac{V_{\text{ferrofluid}}}{N}\right)^{\frac{1}{3}} \quad (7)$$

Finally, the Brownian relaxation time τ_B reads:

$$\tau_B = \frac{3V_h n}{k_B T} \quad (8)$$

where V_h denotes the hydrodynamic volume obtained from the hydrodynamic diameter measured through dynamic light scattering and n the viscosity of the liquid carrier.

After all, and based on eqn (3), three cases can be distinguished regarding the role of dipolar interactions in the frequency factor of the susceptibility dissipative component $\frac{2\pi f \tau}{1 + (2\pi f \tau)^2}$ of MNPs energy losses: (a) when $2\pi f \tau < 1$ dipolar interactions increase P, (b) when $2\pi f \tau = 1$ P is maximum and (c) when $2\pi f \tau > 1$ dipolar interactions decrease P.

The applicability of LRT is also revealed by the ratio between the applied magnetic field amplitude and the anisotropy field ($H_K = 2K/\mu_0 M_s$) of samples. For values $H_0/H_K \ll 1$, the linear response theory can quantify[74] the experimental results. In the present study, for all samples, this ratio was in the order of 10^{-2}.

3.6.2 Evaluation of size effect on heating efficiency. Another parameter that affects SLP values is the size of MNPs. The present study has been designed on that basis and variation of MNPs' size is coming straightforward from the experimental data. Thus, the prediction of the optimum size, *i.e.*, the size that maximizes the heating efficiency of MNPs, by a theoretical approach gives us further evidence for SLP behavior. Employing again the LRT, updated with the import of the mean dipolar energy term of eqn (5) and by substituting in eqn (4)–(8), the samples anisotropy, saturation magnetization and working concentration of 2 mg mL^{-1}, we found the theoretical size of MNPs for which the condition $2\pi f \tau = 1$ is fulfilled for each sample. The results are shown in Fig. 7. For samples S$_1$@Pt, S$_2$@Pt, S$_3$@Pt and S$_4$@Pt, the magnetic core optimum diameters were found equal to be 16, 7, 10 and 20 nm, respectively. By comparing those values to the corresponding experiments, the size of the magnetic core of sample S$_4$@Pt (20 nm) is identical to the optimum one predicted by theory, while all the other samples presented a greater divergence as depicted in Fig. 7. This size is just below the critical single-domain size for ferrite nanoparticles[75] and therefore highly suited to
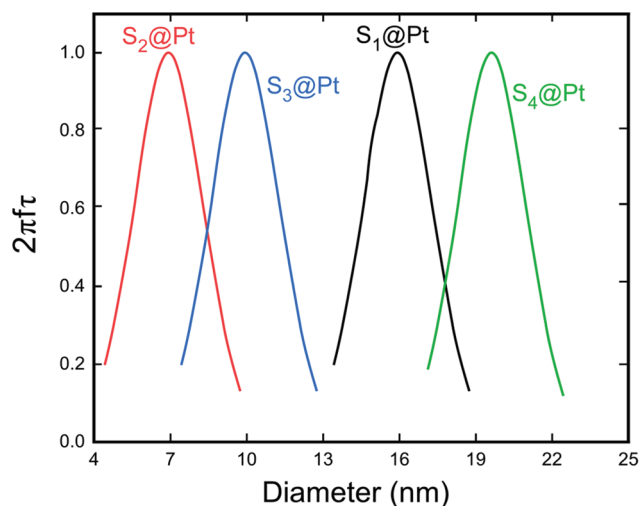
Fig. 7 Dependence of the factor $2\pi f\tau$ on the MNP diameter for the whole set of samples. This maximum corresponds to the resonant size of our MNPs for the working frequency of 765 kHz. The relaxation time τ was calculated by taking into account the Néel and Brown moment relaxation mechanisms that were obtained from eqn (3) and (7), respectively.

Fig. 8 Dependence of the frequency factor $\frac{2\pi f\tau}{1 + (2\pi f\tau)^2}$ of the dissipative susceptibility component on the MNPs concentration for the whole set of samples. This factor shows a sharp maximum at $c = 4$ mg mL^{-1}. This maximum corresponds to the resonant concentration of our MNPs for the working frequency of 765 kHz. This model provides a rigorous estimation of the MNPs concentration that is closer to the optimum condition $2\pi f\tau = 1$ and thus generates higher power losses.

achieve efficient magnetic hyperthermia performance.[76] From the experimental and theoretical results presented so far, we observed systematic supremacy of sample S$_4$@Pt over all other samples concerning their heating efficiency. Except for the optimum size, S$_4$@Pt is also characterized by the lowest anisotropy compared to other samples. This property may also explain the experimental findings since increasing the anisotropy results in attenuation of SLP when MNPs are in the superparamagnetic regime.[68,77] The larger anisotropy implies higher magnetic field amplitudes to achieve a reasonable SLP.

3.6.3 Optimization of concentration. A crucial extrinsic MNP property, that determines inter-particle distances in the colloidal system, is the concentration that arises from eqn (5) and (6) and in turn can affect the dipolar interactions. Thus, it is crucial to find MNPs' optimum concentration that maximises their heating efficiency. By employing eqn (3)–(8), we estimated the susceptibility dissipative component for eight different concentration values (1–8 mg mL^{-1}) and for the working AMF frequency of 765 kHz. The results are illustrated in Fig. 8, where the optimum concentration of theoretical MNPs for the samples after the Pt-complex absorption was found equal to 4 mg mL^{-1}, a value that has been considered well-accepted for MH application.[78–81] Other works have also reached the same qualitative conclusions about the dipolar interaction, namely, that for soft particles, upon increasing the concentration, the SLP first increases up to a point where the dipolar interaction becomes comparable with the anisotropy field, after which it starts to decrease with the concentration.[82–86]

Moreover, Fig. 8 elucidates the SLP attenuation portrayed in Fig. 6b. The addition of PEG and Pt-complex increases the spacing between the nanoparticles and thus decreases the
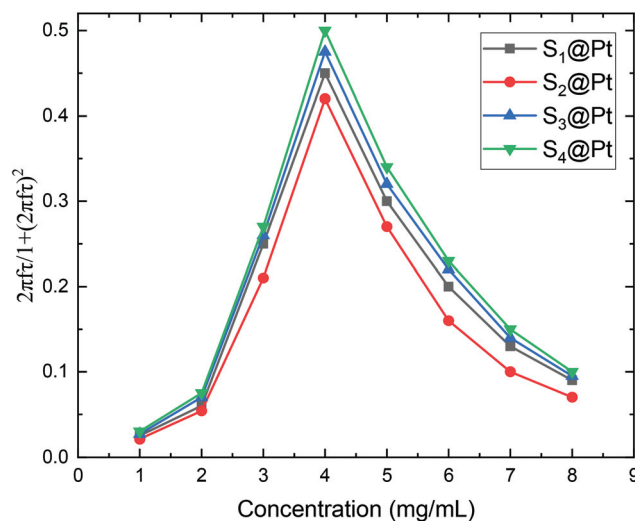
strength of dipolar interactions between them. At low concentrations, like the one used here (2 mg mL^{-1}), this decrease results in the reduction of power dissipation of MNPs as analyzed above and shown in Fig. 6b. When comparing the SLP values among the samples of each concentration, we found that the sample which had the highest saturation magnetization, the largest size, closer to the optimum one, and the lowest effective anisotropy constant value, showed the highest SLP values.

3.6.4 Validation of the theoretical approach. By following this methodology, we aim in rendering theoretical calculations as a two-way process of experimental results evaluation. Thus, after obtaining the optimum concentration, magnetic hyperthermia experimental measurements were conducted in three of the eight, theoretically used, concentrations, and more specifically at 2, 4 and 8 mg mL^{-1} in order to validate our method and confirm experimental heating performance optimization of MNPs. In Fig. 9, the concentration effect on temperature curves is illustrated. The theory-resulted optimum concentration of 4 mg mL^{-1} is verified for all samples. More specifically, at this concentration, S$_1$@Pt, S$_3$@Pt and S$_4$@P samples entered quite fast in MH window at 41–45 °C approaching the temperature safety limit for the optical fiber (60 °C) in less than 600 s.

Consequently, SLP values calculated from eqn (2) are presented in Fig. 10. A good agreement with the theory arises from the fact that SLP behavior is consistent with the frequency factor dependence on the concentration shown in Fig. 8. A deviation from theory is observed in Fig. 10 for samples S$_3$@Pt and S$_4$@Pt at a concentration of 8 mg mL^{-1}, where the SLP of the former is slightly higher than the SLP of the latter. This result is attributed to better dispersion of sample S$_3$@Pt in the high concentration aqueous solution. A
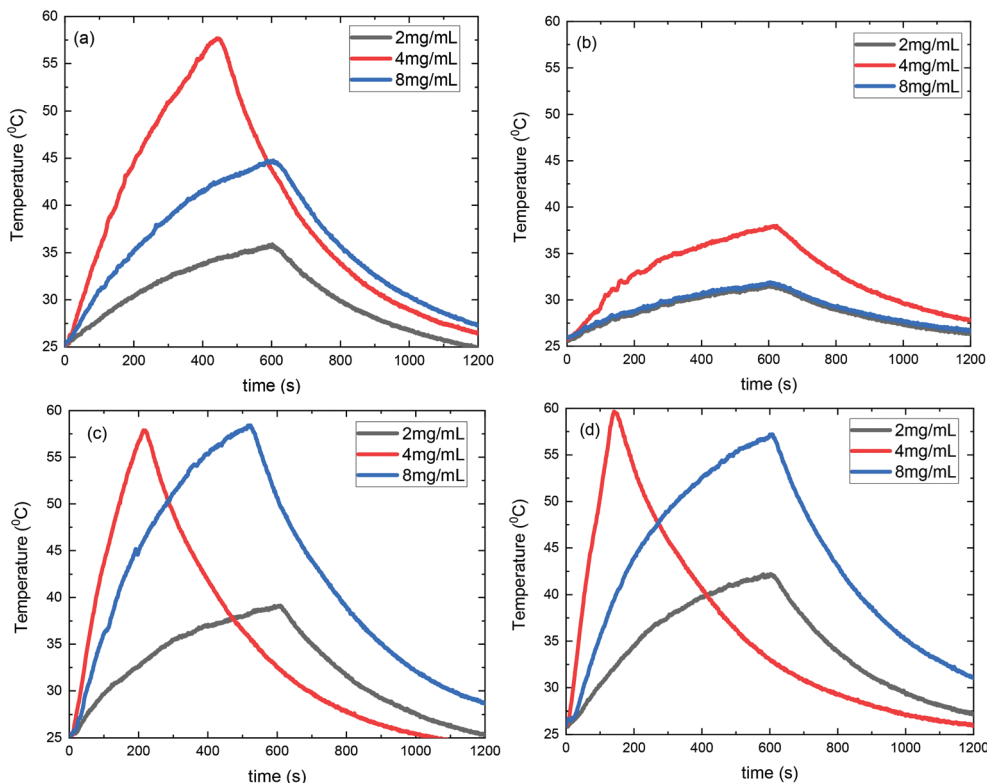
Fig. 9 Experimental curves of heating sequence during MH of (a) S_1@Pt, (b) S_2@Pt, (c) S_3@Pt and (d) S_4@Pt at three different concentration values namely 2, 4 and 8 mg mL^{-1}. AMF amplitude and frequency were set to 24 kA m^{-1} and 765 kHz respectively. The concentration value of 4 mg mL^{-1} presented the higher heating rate verifying theoretical estimations.
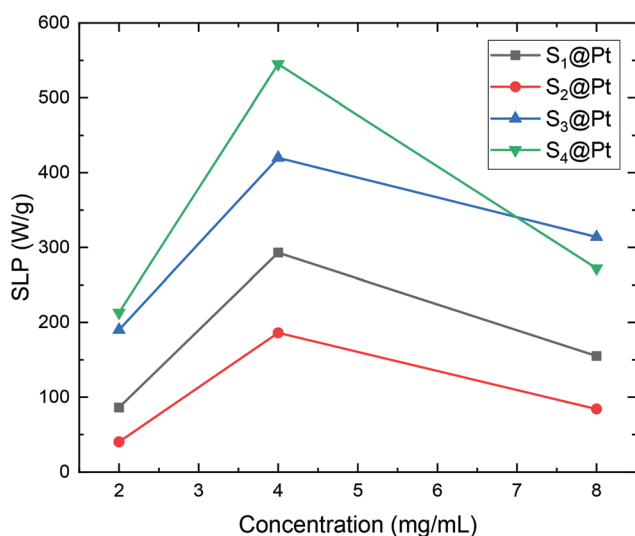

Fig. 10 SLP values of samples S_1@Pt, S_2@Pt, S_3@Pt and S_4@Pt for the three different concentrations (2, 4 and 8 mg mL^{-1}) used in magnetic hyperthermia experiments.

higher dispersion would decrease dipolar interactions between MNPs by increasing inter-particle distance. This tendency is beneficial for the heating efficiency of MNPs at high concentrations, higher than 4 mg mL^{-1}, where decreasing dipolar

interactions increase SLP as expected by theory and shown in Fig. 8.

From our results, it is clear that S_4@Pt and S_3@Pt MNPs presented higher SLP values, 545 W g^{-1} (ILP = 1.25 nHm^2 kg^{-1}) and 420 W g^{-1} (ILP = 0.96 nHm^2 kg^{-1}), respectively, at the optimum concentration compared to the other samples. In any case, all SLP values are considered to be quite adequate, if we also take into account the inevitable reduction due to the addition of Pt-complex, when compared to results attained in the literature on zinc ferrite MNPs.[79,80] Moreover, with the exception of S_2@Pt, all the other samples appeared to be suitable candidates for MH since they surpassed the MH temperature threshold of 41 °C. As indicated by theory, the concentration of 4 mg mL^{-1} generated the highest SLP value compared to 2 and 8 mg mL^{-1}, for all the samples examined, since the quantity $2\pi f\tau$ for those two values deviated significantly from the unit as derived from our calculations. At low concentrations and when σ is low enough, $2\pi f\tau < 1$, the low-barrier regime occurs, where MNPs magnetic moment rotation is frequent, but the released energy in each rotation is small. By raising the concentration, and so the dipolar interactions, the anisotropy barrier increases and thus takes the system closer to the optimum condition $2\pi f\tau = 1$. Conversely, when σ is larger, $2\pi f\tau > 1$, the high-barrier regime appears, where external AMF already has substantial difficulty in promoting the rotations. Thus, the amplification of dipolar interactions through MNPs' concen-

tration, the anisotropy barrier merely increases, even more, hampering further the efficacy of the heating process. This also shows the importance of choosing the appropriate frequency to increase the heating efficiency of high interacting MNPs systems. AMF amplitude of 24 kA m^{-1} used in MH experiments is appropriate for the validity of LRT approximation[28,76] which is extended by using a mean-field model in order to analyze the role of dipolar interactions through the evaluation of MNPs concentration in SLP in the context of MH.

4. Conclusions

Zinc ferrites MNPs ($Zn_xFe_{3-x}O_4$, x = 0.3, 0.4, 0.45, 0.53) with optimal magnetic characteristics for MH have been combined with a Pt-complex as an OFI probe through the *post* and *in situ* PEGylation to form stable hybrid magneto-fluorescent nanocomposites. PEGylation effectively hindered the quenching of emission light and preserved magnetization at high levels. The results of the initial MH measurements showed a sample-oriented-dependent behavior *vis-à-vis* SLP and prompted the application of a theoretical model in order to interpret and optimize them. Thus, the optimum size and concentration that maximize MNP power losses are estimated by theoretical calculations, where the contribution from inter-particle interactions has been considered by inserting a mean dipolar energy term in the estimation of Néel relaxation time. Next, our theoretical approach is validated by further MH outcomes regarding the dependence of time-temperature curves and SLP values on MNPs concentration. In this way, the experimental results are decoded by theory and *vice versa*. Additionally, considering that the primary MNPs presented high relaxivity values r_2,[39] we expect that the current magneto-fluorescent nanocomposites would also be able to perform as a sensitive probe for MRI applications.

Author contributions

Conceptualization, K.V., N.M. and C.D.S.; methodology, K.V. and N.M.; formal analysis, K.V. and N.M.; investigation, K.V. and N.M.; resources, K.V. and N.M.; data curation, K.V. and N.M.; writing-original draft preparation, K.V. and N.M.; writing-review & editing, K.V., N.M. and C.D.S.; supervision, C.D.S. All authors have read and agreed to the published version of the manuscript.

Conflicts of interest

The authors declare no conflict of interest.

Acknowledgements

References

1 N. Knežević, I. Gadjanski and J. O. Durand, *J. Mater. Chem. B*, 2019, **7**, 9–23.
2 G. Chen, I. Roy, C. Yang and P. N. Prasad, *Chem. Rev.*, 2016, **116**, 2826–2885.
3 J. Zhao, J. Chen, S. Ma, Q. Liu, L. Huang, X. Chen, K. Lou and W. Wang, *Acta Pharm. Sin. B*, 2018, **8**, 320–338.
4 E. K. Lim, T. Kim, S. Paik, S. Haam, Y. M. Huh and K. Lee, *Chem. Rev.*, 2015, **115**, 327–394.
5 Z. Liu, X. Zhan, M. Yang, Q. Yang, X. Xu, F. Lan, Y. Wu and Z. Gu, *Nanoscale*, 2016, **8**, 7544–7555.
6 L. Lartigue, C. Innocenti, T. Kalaivani, A. Awwad, M. D. M. Sanchez Duque, Y. Guari, J. Larionova, C. Gueírin, J. L. G. Montero, V. Barragan-Montero, P. Arosio, A. Lascialfari, D. Gatteschi and C. Sangregorio, *J. Am. Chem. Soc.*, 2011, **133**, 10459–10472.
7 C. G. Hadjipanayis, M. J. Bonder, S. Balakrishnan, X. Wang, H. Mao and G. C. Hadjipanayis, *Small*, 2008, **4**, 1925–1929.
8 F. Stuker, J. Ripoll and M. Rudin, *Pharmaceutics*, 2011, **3.2**, 229–274.
9 E. J. Sutton, T. D. Henning, S. Boddington, S. Demos, C. Krug, R. Meier, J. Kornak, S. Zhao, R. Baehner, S. Sharifi and H. Daldrup-Link, *Mol. Imaging*, 2010, **9**, 278–290.
10 W. Stummer, U. Pichlmeier, T. Meinel, O. D. Wiestler, F. Zanella and H. J. Reulen, *Lancet Oncol.*, 2006, **7**, 392–401.
11 L. Bu, B. Shen and Z. Cheng, *Adv. Drug Delivery Rev.*, 2014, **76**, 21–38.
12 G. M. Van Dam, G. Themelis, L. M. A. Crane, N. J. Harlaar, R. G. Pleijhuis, W. Kelder, A. Sarantopoulos, J. S. De Jong, H. J. G. Arts, A. G. J. Van Der Zee, J. Bart, P. S. Low and V. Ntziachristos, *Nat. Med.*, 2011, **17**, 1315–1319, DOI: 10.1038/nm.2472.
13 W. J. M. Mulder, G. J. Strijkers, G. A. F. Van Tilborg, D. P. Cormode, Z. A. Fayad and K. Nicolay, *Acc. Chem. Res.*, 2009, **42**, 904–914.
14 N. Li, H. Li, D. Chen, H. Liu, F. Tang, Y. Zhang, J. Ren and Y. Li, *J. Nanosci. Nanotechnol.*, 2009, **9**, 2540–2545.
15 S. A. Corr, Y. P. Rakovich and Y. K. Gun'Ko, *Nanoscale Res. Lett.*, 2008, **3**, 87–104, DOI: 10.1007/s11671-008-9122-8.
16 T. T. Jiang, N. Q. Yin, L. Liu, J. M. Lei, L. X. Zhu and X. L. Xu, *Chin. Phys. B*, 2013, **22**, 126102–126102.
17 N. Chekina, D. Horák, P. Jendelová, M. Trchová, M. J. Bene, M. Hrubý, V. Herynek, K. Turnovcová and E. Syková, *J. Mater. Chem.*, 2011, **21.21**, 7630–7639, DOI: 10.1039/c1jm10621j.
18 A. Louie, *Chem. Rev.*, 2010, **110.5**, 3146–3195, DOI: 10.1021/cr9003538.

19 M. K. Yoo, I. K. Park, H. T. Lim, S. J. Lee, H. L. Jiang, Y. K. Kim, Y. J. Choi, M. H. Cho and C. S. Cho, *Acta Biomater.*, 2012, **8.8**, 3005–3013, DOI: 10.1016/j.actbio.2012.04.029.

20 G. Wang and X. Su, *Analyst*, 2011, **136.9**, 1783–1798.

21 A. Quarta, R. Di Corato, L. Manna, A. Ragusa and T. Pellegrino, *IEEE Trans. Nanobioscience*, 2007, **6.4**, 298–308.

22 C. Kaewsaneha, P. Tangboriboonrat, D. Polpanich and A. Elaissari, *ACS Appl. Mater. Interfaces*, 2015, **7.42**, 23373–23386.

23 D. Vollath, *Adv. Mater.*, 2010, **22.39**, 4410–4415, DOI: 10.1002/adma.201001743.

24 C. F. Markwalter, A. G. Kantor, C. P. Moore, K. A. Richardson and D. W. Wright, *Chem. Rev.*, 2019, **119.2**, 1456–1518.

25 K. Cheng, S. Peng, C. Xu and S. Sun, *J. Am. Chem. Soc.*, 2009, **131.30**, 10637–10644, DOI: 10.1021/ja903300f.

26 J. Hernández-Gil, M. Cobaleda-Siles, A. Zabaleta, L. Salassa, J. Calvo and J. C. Mareque-Rivas, *Adv. Healthcare Mater.*, 2015, **4.7**, 1034–1042, DOI: 10.1002/adhm.201500080.

27 E. Voulgari, A. Bakandritsos, S. Galtsidis, V. Zoumpourlis, B. P. Burke, G. S. Clemente, C. Cawthorne, S. J. Archibald, J. Tuček, R. Zbořil, V. Kantarelou, A. G. Karydas and K. Avgoustakis, *J. Controlled Release*, 2016, **243**, 342–356, DOI: 10.1016/j.jconrel.2016.10.021.

28 C. Iacovita, G. F. Stiufiuc, R. Dudric, N. Vedeanu, R. Tetean, R. I. Stiufiuc and C. M. Lucaciu, *Magnetochemistry*, 2020, **6**, 23.

29 A. Das, S. Mohanty, R. Kumar and B. K. Kuanr, *ACS Appl. Mater. Interfaces*, 2020, **12**, 42016–42029.

30 Y. Xu, A. Karmakar, D. Wang, M. W. Mahmood, F. Watanabe, Y. Zhang, A. Fejleh, P. Fejleh, Z. Li, G. Kannarpady, S. Ali, A. R. Biris and A. S. Biris, *J. Phys. Chem. C*, 2010, **114.11**, 5020–5026, DOI: 10.1021/jp9103036.

31 E. K. Lim, J. Yang, C. P. N. Dinney, J. S. Suh, Y. M. Huh and S. Haam, *Biomaterials*, 2010, **31.35**, 9310–9319, DOI: 10.1016/j.biomaterials.

32 C. W. Lai, Y. H. Wang, C. H. Lai, M. J. Yang, C. Y. Chen, P. T. Chou, C. S. Chan, Y. Chi, Y. C. Chen and J. K. Hsiao, *Small*, 2008, **4.2**, 218–224, DOI: 10.1002/smll.200700283.

33 B. Xia, J. Li, J. Shi, Y. Zhang, Q. Zhang, Z. Chen and B. Wang, *ACS Biomater. Sci. Eng.*, 2017, **3**, 2579–2587.

34 A. Z. M. Badruddoza, M. T. Rahman, S. Ghosh, M. Z. Hossain, J. Shi, K. Hidajat and M. S. Uddin, *Carbohydr. Polym.*, 2013, **95.1**, 449–457, DOI: 10.1016/j.carbpol.2013.02.046.

35 M. J. Sailor and E. J. Lee, *Adv. Mater.*, 1997, **9.10**, 783–793, DOI: 10.1002/adma.19970091004.

36 J. M. Buriak, *Chem. Rev.*, 2002, **102**, 1271–1308.

37 S. Ciampi, J. B. Harper and J. J. Gooding, *Chem. Soc. Rev.*, 2010, **39**, 2158–2183.

38 L. Li, C. Liu, L. Zhang, T. Wang, H. Yu, C. Wang and Z. Su, *Nanoscale*, 2013, **5**, 2249–2253.

39 P. Sun, H. Zhang, C. Liu, J. Fang, M. Wang, J. Chen, J. Zhang, C. Mao and S. Xu, *Langmuir*, 2010, **26.2**, 1278–1284, DOI: 10.1021/la9024553.

40 K. Giannousi, O. Antonoglou and C. Dendrinou-Samara, *ACS Chem. Neurosci.*, 2019, **10**, 3796–3804.

41 Y. herng Chen, J. W. Merkert, Z. Murtaza, C. Woods and D. P. Rillema, *Inorg. Chim. Acta*, 1995, **240**, 41–47.

42 R. B. Bostancıoğlu, K. Işık, H. Genç, K. Benkli and A. T. Koparal, *J. Enzyme Inhib. Med. Chem.*, 2012, **27**, 458–466.

43 K. Vamvakidis, M. Katsikini, G. Vourlias, M. Angelakeris, E. C. Paloura and C. Dendrinou-Samara, *Dalton Trans.*, 2015, **44**, 5396–5406.

44 F. A. Palocsay and J. V. Rund, *Inorg. Chem.*, 1969, **8.3**, 524–528, DOI: 10.1021/ic50073a022.

45 M. Angelakeris, *Biochim. Biophys. Acta, Gen. Subj.*, 2017, **1861.6**, 1642–1651.

46 A. J. Biacchi and R. E. Schaak, The Solvent Matters: Kinetic versus Thermodynamic Shape Control in the Polyol Synthesis of Rhodium Nanoparticles, *ACS Nano*, 2011, **10**, 8089–8099.

47 X. Wang, G. Jia, Y. Yu, Y. Gao, W. Zhang, H. Wang, Z. Cao and J. Liu, *Quim. Nova*, 2015, **38**, 298–302.

48 X. Wang, G. Jia, Y. Yu, Y. Gao, W. Zhang, H. Wang, Z. Cao and J. Liu, *Quim. Nova*, 2015, **38**, 298–302.

49 V. Wagner, A. Dullaart, A. K. Bock and A. Zweck, *Nat. Biotechnol.*, 2006, **24**, 1211–1217.

50 J. S. Suka, Q. Xua, N. Kima, J. Hanesa and L. M. Ensigna, PEGylation as a strategy for improving nanoparticle-based drug and gene delivery, *Adv. Drug Delivery Rev.*, 2016, **99**, 28–51.

51 C. F. Bohren and D. R. Huffman, *Absorption and Scattering of Light by Small Particles*, Wiley, 1998.

52 F. P. Dwyer and E. C. Gyarfas, Chelate complexes of 1,10-phenanthroline and related compounds, *Chem. Rev.*, 1954, **54**, 959–1017.

53 P. Xi, K. Cheng, X. Sun, Z. Zeng and S. Sun, Fluorescent magnetic nanoparticles based on a ruthenium complex and Fe3O4, *J. Mater. Chem.*, 2011, **21**, 11464–11467.

54 S. P. Yeap, J. Lim, B. S. Ooi, *et al.*, Agglomeration, colloidal stability, and magnetic separation of magnetic nanoparticles: collective influences on environmental engineering applications, *J. Nanopart. Res.*, 2017, **19**, 368.

55 P. M. Zélis, G. A. Pasquevich, S. J. Stewart, M. B. F. Van Raap, J. Aphesteguy, I. J. Bruvera, C. Laborde, B. Pianciola, S. Jacobo and F. H. Sánchez, *J. Phys. D: Appl. Phys.*, 2013, **46**, 125006.

56 X. Liu, J. Liu, S. Zhang, Z. Nan and Q. Shi, *J. Phys. Chem. C*, 2016, **120**, 1328–1341.

57 Y. Hadadian, A. P. Ramos and T. Z. Pavan, *Sci. Rep.*, 2019, **9.1**, 1–14, DOI: 10.1038/s41598-019-54250-7.

58 O. Yelenich, S. Solopan, T. Kolodiazhnyi, Y. Tykhonenko, A. Tovstolytkin and A. Belous, *J. Chem.*, 2015, 532198, DOI: 10.1155/2015/532198.

59 S. K. Sharma, *Complex magnetic nanostructures: Synthesis, assembly and applications*, Springer International Publishing, 2017.

60 J. Herbst and F. Pinkerton, *Phys. Rev. B: Condens. Matter Mater. Phys.*, 1998, **57**, 10733–10739.

61 M. Thakur, K. De, S. Giri, S. Si, A. Kotal and K. Mandali, *J. Phys.: Condens. Matter*, 2008, **20**, 149801.

62 N. Modaresi, R. Afzalzadeh, B. Aslibeiki, P. Kameli, A. Ghotbi Varzaneh, I. Orue and V. A. Chernenko, *J. Magn. Magn. Mater.*, 2019, **482**, 206–218.

63 A. Goldman, *Handbook of Modern Ferromagnetic Materials*, Springer US, 1999.

64 F. Bødker, S. Mørup and S. Linderoth, *Phys. Rev. Lett.*, 1994, **72**, 282–285.

65 F. Gazeau, J. C. Bacri, F. Gendron, R. Perzynski, Y. L. Raikher, V. I. Stepanov and E. Dubois, *J. Magn. Magn. Mater.*, 1998, **186**, 175–187.

66 A. A. McGhie, C. Marquina, K. O'Grady and G. Vallejo-Fernandez, *J. Phys. D: Appl. Phys.*, 2017, **50**, 455003.

67 A. Das, S. Mohanty, R. Kumar and B. K. Kuanr, *ACS Appl. Mater. Interfaces*, 2020, **12**, 42016–42029.

68 A. Rajan, M. Sharma and N. K. Sahu, *Sci. Rep.*, 2020, **10**, 15045, DOI: 10.1038/s41598-020-71703-6.

69 R. R. Shah, T. P. Davis, A. L. Glover, D. E. Nikles and C. S. Brazel, *J. Magn. Magn. Mater.*, 2015, **387**, 96–106.

70 R. P. Tan, J. Carrey and M. Respaud, *Phys. Rev. B: Condens. Matter Mater. Phys.*, 2014, **90**, 214421.

71 B. Mehdaoui, R. P. Tan, A. Meffre, J. Carrey, S. Lachaize, B. Chaudret and M. Respaud, *Phys. Rev. B: Condens. Matter Mater. Phys.*, 2013, **87**, 174419.

72 R. E. Rosensweig, *J. Magn. Magn. Mater.*, 2002, **252**, 370–374, DOI: 10.1016/S0304-8853(02)00706-0.

73 G. T. Landi, *Phys. Rev. B: Condens. Matter Mater. Phys.*, 2014, **89**, 014403.

74 S. Ruta, R. Chantrell and O. Hovorka, *Sci. Rep.*, 2015, **5**, 1–7.

75 I. Hilger, *Int. J. Hyperthermia*, 2013, **29.8**, 828–834.

76 X. L. Liu, H. M. Fan, J. B. Yi, Y. Yang, E. S. G. Choo, J. M. Xue, D. Di Fan and J. Ding, *J. Mater. Chem.*, 2012, **22**, 8235–8244.

77 J. Carrey, B. Mehdaoui and M. Respaud, *J. Appl. Phys.*, 2011, **109**, 083921.

78 A. LeBrun, R. Ma and L. Zhu, *J. Therm. Biol.*, 2016, **62**, 129–137.

79 E. Myrovali, N. Maniotis, T. Samaras and M. Angelakeris, *Nanoscale Adv.*, 2020, **2**, 408–416.

80 H. F. Rodrigues, G. Capistrano, F. M. Mello, N. Zufelato, E. Silveira-Lacerda and A. F. Bakuzis, *Phys. Med. Biol.*, 2017, **62**, 4062–4082.

81 A. Skumiel, K. Kaczmarek, D. Flak, M. Rajnak, I. Antal and H. Brząkała, *J. Mol. Liq.*, 2020, **304**, 112734.

82 P. Appa Rao, K. Srinivasa Rao, T. R. K. Pydi Raju, G. Kapusetti, M. Choppadandi, M. Chaitanya Varma and K. H. Rao, *J. Alloys Compd.*, 2019, **794**, 60–67.

83 M. S. A. Darwish, H. Kim, H. Lee, C. Ryu, J. Y. Lee and J. Yoon, *Nanomaterials*, 2019, **9**, 1176.

84 C. Martinez-Boubeta, K. Simeonidis, D. Serantes, I. Conde-Leborán, I. Kazakis, G. Stefanou, L. Peña, R. Galceran, L. Balcells, C. Monty, D. Baldomir, M. Mitrakas and M. Angelakeris, *Adv. Funct. Mater.*, 2012, **22**, 3737–3744.

85 J. w. Kim, J. Wang, H. Kim and S. Bae, Concentration-dependent oscillation of specific loss power in magnetic nanofluid hyperthermia, *Sci. Rep.*, 2021, **11**, 733.

86 J. G. Ovejero, D. Cabrera, J. Carrey and T. Valdivielso, Effects of inter-and intra-aggregate magnetic dipolar interactions on the magnetic heating efficiency of iron oxide nanoparticles, *Phys. Chem. Chem. Phys.*, 2016, **18**, 10954–10963.